2023-03-01

Release of tephra-hosted iron during early diagenesis fingerprinted by iron isotopes

Longman, J

10.1016/j.epsl.2023.118016
Earth and Planetary Science Letters
Elsevier BV

Release of tephra-hosted iron during early diagenesis fingerprinted by iron isotopes

Jack Longman[1], Ann G. Dunlea[2], Philipp Böning[1], Martin R. Palmer[3], Thomas M. Gernon[3], James McManus[4], Hayley R. Manners[5], William B. Homoky[6], Katharina Pahnke[1]

[1]Marine Isotope Geochemistry, Institute for Chemistry and Biology of the Marine Environment (ICBM), University of Oldenburg, Oldenburg, Germany

[2]Woods Hole Oceanographic Institution, Woods Hole, MA, USA.

[3]School of Ocean and Earth Sciences, University of Southampton, Southampton, UK

[4]Bigelow Laboratory for Ocean Sciences, East Boothbay, ME, USA.

[5]School of Geography, Earth and Environmental Sciences, University of Plymouth, Plymouth, UK.

[6]School of Earth and Environment, University of Leeds, Leeds, UK

Abstract

The micronutrient iron (Fe) plays a fundamental role controlling primary productivity in the upper ocean, with volcanic eruptions and deposition of airborne volcanic material (termed tephra) a potential source of Fe. Here, we investigate the geochemical and Fe isotopic (δ^{56}Fe) composition of tephra layers, sediments, and mixed tephra-sediment samples from the Integrated Ocean Drilling Program (IODP) Hole 1396C, located offshore the volcanically active island of Montserrat in the Lesser Antilles, Caribbean Sea. We find that buried tephras, which have experienced diagenesis, exhibit lighter δ^{56}Fe (relative to standard IRMM-524a) compositions (down to -0.26 ± 0.04‰, 2SD) than fresh tephra deposited on Montserrat (δ^{56}Fe = 0.02 ± 0.02‰, 2SD). Such negative values suggest that isotopically heavier Fe has been lost from the originally deposited material. Using multivariate statistical modelling and mass balance constraints, we identify the outward Fe flux (with calculated δ^{56}Fe of 0.21 ± 0.31‰, 2SD, n=12) during non-reductive dissolution of tephra as the likely cause of the retention of these light δ^{56}Fe compositions. Due to the widespread nature of tephra deposition, tephra diagenesis may provide an important source of isotopically heavy dissolved Fe to the oceans. This process contrasts with more commonly considered reductive dissolution processes, which provide a source of Fe enriched in light isotopes to the oceans.

Introduction

As an essential micronutrient for phytoplankton photosynthesis, iron (Fe)availability is directly linked to primary productivity and plankton community structure in modern high-latitude oceans (Falkowski et al., 1998; Kolber et al., 1994; Martin and Fitzwater, 1988; Tagliabue et al., 2017). Because primary productivity is one of the most important mechanisms determining air-sea CO_2 exchange, understanding Fe biogeochemistry is key to understanding marine carbon cycling (Tagliabue et al., 2017).

Fe is supplied to the ocean via rivers, aeolian deposition, hydrothermal vents and remobilisation of sediment-hosted Fe (Homoky et al., 2013; Johnson et al., 2020; König et al., 2021). In addition, volcanism, and especially the eruptive dispersal of tephra, may provide an important episodic input of Fe to the Earth's surface environment (Longman et al., 2022; Olgun et al., 2011). Explosive volcanism results in the total eruption of ~1 km^3 of tephra (or unconsolidated pyroclastic material including pore space) every year (Pyle, 1995), and because most volcanoes are located islands or near continental margins, as much as 45% of this tephra enters the ocean (Longman et al., 2022). Upon entering the ocean, tephra reacts rapidly with seawater, releasing large quantities of macro- and micro-nutrients such as Fe (Frogner et al., 2001; Jones and Gislason, 2008). A first estimate of the scale of this nutrient supply indicates tephra may deliver between 50 – 500 Gmol yr^{-1} of Fe to the oceans, with a median value of 180 Gmol yr^{-1} (Longman et al., 2022). The Fe delivery associated with tephra could therefore alleviate nutrient deficiencies for phytoplankton in Fe-limited regions of the ocean (Achterberg et al., 2013; Duggen et al., 2010; Moore et al., 2013; Olgun et al., 2013). Further, the release of other micronutrients such as Mn during this process mean tephra may also supply other co-limiting nutrients (Browning et al., 2021, 2014; Longman et al., 2020). The magnitude of this Fe source is also highlighted by the observation that roughly 30% of Pacific sediment located close (within 1000km) active arcs is comprised of tephra (Scudder et al., 2014, 2009). However, despite the potential importance to oceanic Fe budgets, the supply of Fe from diagenesis of volcanic material within the sediment is poorly constrained and not explicitly represented in ocean biogeochemical models of Fe (König et al., 2021; Tagliabue et al., 2016).

One method for investigating the cycling of Fe in the ocean uses its isotopic composition, typically presented as δ^{56}Fe relative to a measured standard. This composition can help trace the sources, sinks and fluxes of Fe in the oceans and sediments (Conway and John, 2014; Homoky et al., 2013; Radic et al., 2011), provided the external sources of dissolved (Fe in solution; dFe) and particulate (Fe associated with particles >0.2μm; pFe) Fe to the oceans and the processes that fractionate Fe isotopes within the ocean system are understood (Johnson et al., 2020).

Typically, sources of Fe to the ocean such as dust and Fe release from oxic sediment, have isotopic signatures close to crustal values (0.09 ± 0.07‰; Beard et al., 2003). However, these compositions may be modified in parts of the ocean influenced by variable redox conditions (Johnson et al., 2020). For example, in low-oxygen sedimentary environments, reductive dissolution of Fe (a product of dissimilatory microbial reactions) leads to the release of negative δ^{56}Fe compositions to porewaters, with values reaching as low as -3.3‰ (Homoky et al., 2009). Hydrothermal vent fluids typically have δ^{56}Fe between -0.1 to -0.5‰ (Bennett et al., 2009; Johnson et al., 2020), but can be modified by the precipitation of sulfides or oxides. These precipitation reactions occur when either of the species are saturated in the fluids, with precipitates preferentially incorporating lighter (when sulfides form) and heavier isotopes (when oxides form), thereby fractionating the Fe which remains in the fluid (Lough et al., 2017).

In addition to these reductive dissolution pathways, heavy (δ^{56}Fe > 0‰) lithogenic Fe signatures have been observed in porewaters (Homoky et al., 2013; 2021) and seawater (Conway and John, 2014; Radic et al., 2011) in some deep water locations. This has been attributed to non-reductive dissolution (NRD) of lithogenic material in oxidising sediments, and indicates these oxic sediments may be an additional source of dFe to the oceans (Abadie et al., 2017; Homoky et al., 2013; König et al., 2021). This process, via the production of organomineral Fe colloids, may provide a mechanism by which lithogenic δ^{56}Fe compositions are added to the ocean interior from oxidising margins (Homoky et al., 2021). Notably, the oxidative weathering of volcanoclastic material containing high organic carbon content (>1%) produces porewater with the highest concentration of Fe colloids with crustal isotope compositions (Homoky et al., 2021).

Here, we present Fe isotopic compositions from sediments, tephras and mixed sediment-tephra layers from offshore Montserrat in the Caribbean Sea to estimate the Fe isotopic composition of Fe lost during tephra diagenesis. We combine these data with multivariate partitioning methods and calculations of the depletion factors and mass balance calculations to estimate the isotopic composition of Fe supplied to the ocean via dissolution of tephra during water column transport and early diagenesis.

Methods

Study Site, Sampling and Age Model

Integrated Ocean Drilling Program (IODP) Hole 1396C was drilled as part of Expedition 340 in August-September 2012 (Le Friant et al., 2013). It is located ~30 km west of Montserrat at 16°30.5′N, 62°27.1′W (Fig. 1), and was drilled to a depth of 139.4 m below seafloor (mbsf). The core is carbonate-dominated, with abundant tephra layers and a minor contribution from terrigenous sediments. Bulk marine sediment and visually distinct discrete tephra layers were both sampled. For the samples from the tephra layers, efforts were made to sample from the centre of the layer to attain a purely volcanic signal. In addition to the IODP samples, we also studied fresh tephra from the 8th January 2010 eruption of the Soufrière Hills volcano, Montserrat.

Elemental analysis

Freeze-dried and homogenized tephra (n=18) and sediment (n=44) samples were dissolved using a mixed acid (HCl-HF-HNO_3) benchtop method. Solutions were diluted 1:5000 and analysed using a Thermo X-Series at the University of Southampton following the protocol of Longman et al. (2022). The certified reference material HISS-1 (sandy marine sediment), and procedural blanks were prepared and analysed in the same manner. For this work, a full suite of major and trace elements was analysed. Blank content was shown to be negligible for all elements, and recoveries for HISS-1 were within 10% of expected values for most elements (see Supplementary Table 1). For Fe, 2 measurements of HISS-1 averaged 2950 ppm, with an expected value of 2460 (recovery 97%). Blanks for Fe were on average 0.66 ppm, or 0.02% of the standard material. Porewater analysis of Fe was completed using the method of Murray et al. (2016). Briefly, pore waters were diluted to a 1:20 ratio using 1% distilled nitric acid

before analysis on a Leeman Labs Prodigy ICP-OES at Oregon State University. The fresh tephra was analysed via X-Ray Fluorescence (Philips PW 2400) analysis at the University of Oldenburg. 600mg of sample was mixed with 3600 mg of a 1:1 dilithiumtetraborate:lithiummetaborate mixture, pre-oxidised at 500 °C with NH_4NO_3 and fused to form a glass bead. The in-house standard PS_S was prepared an analysed in the same manner. Fe_2O_3 content in the measured standard was 4.91%, compared to a long-term average of 4.76%.

Carbon analyses

Total organic carbon (TOC) measurements were made at Oregon State University following the method of Goñi et al. (2003), as reported in Murray et al. (2016). Further details on methods, blanks and reproducibility can be found in Murray et al. (2016).

Fe isotope analysis

A portion of the samples analysed for major and trace elements, and the fresh tephra sample, were analysed for their Fe isotope composition (n = 20). Samples were homogenized using an agate pestle and mortar prior to digestion of around 25mg of sample via a mixed acid (HNO_3-$HClO_4$-HF) closed-vessel approach (Böning et al., 2004). Blanks and certified reference materials were dissolved in the same manner as samples. Aliquots of the digested samples were then purified via column chemistry (Böning et al., 2020; Dauphas et al., 2009). Samples were taken up in 6M HCl and Fe separation was performed using 1.8 mL AG1X8 anion resin (100–200 mesh, Bio-Rad) loaded onto PP columns (Bio-Rad). After separation, samples were treated with H_2O_2 to remove any organic compounds leached from the columns, before drying. All purification was completed using ultra-clean acids in the clean laboratory facilities of the ICBM, University of Oldenburg.

Purified samples were diluted (to 3% HNO_3 and 3.3 ppm Fe) and analysed using a Thermo-Scientific Neptune *Plus* multi-collector inductively coupled plasma mass spectrometer (MC-ICP-MS) at the ICBM, Oldenburg. NIST 986 (National Institute of Standards and Technology, USA), a certified Ni isotope standard, was quantitatively added to each sample and standard for mass bias correction (Oeser et al., 2014). Signal intensity was ~15V for Fe and ~3V for Ni. Interference of ^{54}Cr on ^{54}Fe was

monitored and corrected using ^{52}Cr (Weyer and Schwieters, 2003). Analysis of each sample was bracketed by a repeat standard (IRMM-524a), which is indistinguishable (within experimental uncertainty) from the more widely used isotope standard IRMM-14 (González De Vega et al., 2020). All results and comparisons to the literature are reported in delta notation relative to the mean of repeat IRMM-524 values (n= 112):

$$\delta^{56}Fe\ (‰) = [(^{56}Fe/^{54}Fe_{sample})/(^{56}Fe/^{54}Fe_{IRMM\text{-}524})] * 10^3$$

The reference materials SDO-1 (Devonian shale, US Geological Survey), BHVO-2 (Hawaiian basalt, US Geological Survey) and HISS-1 (marine sandy sediment, National Research Council of Canada) were used to assess the accuracy of Fe separations and measurements. Measurements of SDO-1 ($\delta^{56}Fe$ = 0.027 ± 0.017‰, n=10, two digests, 2SD) were in good agreement with published values of 0.023 ± 0.028‰ (Schoenberg and Von Blanckenburg, 2005), and 0.026 ± 0.045‰ (Böning et al., 2020). Measurements of BHVO-2 ($\delta^{56}Fe$ = 0.078 ± 0.041‰, n=3, 2SD) were within error of previously published values of 0.121 ± 0.049‰ (Liu et al., 2014), and 0.100 ± 0.060‰ (Foden et al., 2018). Procedural blanks were negligible (<0.1% of total Fe in the lowest concentration sample).

Numerical analysis

Multivariate Partitioning

We used a series of multivariate techniques to determine the sediment provenance and the relative contribution of each source to the sediment mixture deposited at Hole U1396C. First, we assessed the relationships between element concentrations with r^2 matrices, x versus y element plots, and ternary plots to identify trends, outliers, and simple covariation patterns (Supplementary Figures 1-5). Second, we selected elements in the dataset that were predominantly affiliated with the aluminosilicate fraction of the sediment and applied Q-mode Factor Analysis (QFA; Pisias et al., 2013). To ensure the robustness of the QFA results, we tested many combinations of elements, ran iterations with sample outliers removed, and assessed the sensitivity of the results when an additional factor was added or subtracted. Furthermore, we selected elements that were unique from those used in our tephra depletion model (Zr, Ti; see below) to determine if an independent technique produced similar results. Guided by the x versus

y plots, ternary diagrams, and QFA results, elements and end-members were selected on the basis that they could be statistically differentiated in the dataset. The element concentration data were then modelled using constrained-least squares multiple linear regression (CLS; Pisias et al., 2013; Dunlea et al., 2015; Dunlea and Murray, 2015).

In the CLS mixing models, thousands of combinations of possible end-members from published studies or discrete layers measured in this study were tested to best fit the geochemical dataset in this study. The CLS model aims to minimize the difference between the model and measured data. Our preferred model was selected based on the strength of correlation coefficients of the CLS model and our geological knowledge of which sediment sources would feasibly be found at Hole U1396C (see Supplementary Tales. 5-9, Supplementary Text).

Tephra Fe depletion calculations

We used two approaches to calculate early diagenetic Fe depletion factors for samples that were tephra-rich (>75% tephra contribution as estimated from the CLS model): Zr-normalisation after Lee et al. (2018), and a multivariate CLS model. Zr-normalisation compares the Fe/Zr and Ti/Zr ratios of the analysed ashes to a reference dataset of Caribbean volcanic rocks, derived from the GeoROC database (c.f. Longman et al., 2021; Longman et al., 2022). Data were downloaded from https://georoc.eu/, with all original publications and the specific search terms listed in the Supplementary Text. Here, Zr and Zr/Ti are assumed to be immobile whereas Fe may be mobilised during early diagenesis (Lee et al., 2018). The linear regression between the Fe/Zr and Ti/Zr of the igneous rock dataset is interpreted to represent the unaltered protolith of the tephra analysed here (Supplementary Figure 1). Using this relationship and the measured Ti/Zr of the tephra layers, an original Fe/Zr composition can be back-calculated, and depletion factors (DF) estimated, using the following equation:

$$DF_{Fe} = \frac{M_{Fe}^{L}}{M_{Fe}^{O}} = 1 - \frac{\left(\frac{C_{Fe}^{re}}{C_{Zr}^{re}}\right)}{\left(\frac{C_{Fe}^{O}}{C_{Zr}^{O}}\right)} \quad \text{(Eq. 1)}$$

Where the left side of the equation is the Fe depletion factor, DF_{Fe} (in %), with M_{Fe}^{O} the original Fe mass in the protolith and with M_{Fe}^{L} the mass of Fe lost from the protolith C_{Fe}^{re} and C_{Zr}^{re} are the mass concentrations of Fe and Zr in analysed tephra, and C_{Fe}^{O}/C_{Zr}^{O} represents the Fe/Zr ratio of the protolith. All masses are in wt%, with oxide content corrected where necessary.

A second approach, based on the end-member compositions and mass fractions from the CLS model was also applied to the discrete tephra layer and bulk sediment samples. The mass fraction of each end-member within each sample was multiplied by the concentration of Fe in that end-member. Summing the contributions of Fe from each end-member provides an estimate of how much Fe is expected in each sample if no Fe had been lost from the original tephra composition. As such, the total measured Fe in the sample can be subtracted from the predicted Fe content to obtain a depleted fraction:

$$f_{EM1}*[Fe]_{EM1} + f_{EM2}*[Fe]_{EM2} + f_{EM3}*[Fe]_{EM3} = \text{Total } [Fe]_{tephra} \quad \text{(Eq. 2)}$$

where f_{EM} = the fraction (0-1) of an end-member present in tephra. The difference between the predicted total Fe concentration in tephra (Total $[Fe]_{tephra}$) and the independently measured Fe content in tephra and sediment samples provides an estimate of the total Fe (wt. %) lost or gained during early diagenesis.

Results and Discussion

Sources of sediment in Hole U1396C

The multivariate statistical analyses identified three end-members defined from the major and trace metal dataset in the aluminosilicate fraction (i.e., non-carbonate component) of sediment at Hole U1396C. Because the Al and Ti concentrations are much higher than the concentrations of the other trace elements, they have more influence on the outcome of the model. For example, the magnitude of a small variation in Al can still be much larger than a relatively significant variation in Nb. To avoid this bias toward higher concentration elements, we did not use Al and Ti in the CLS model and instead relied on elements in the ppm range. The factor analysis suggests that three aluminosilicate components can be distinguished with or without Al and Ti included. In our preferred model, the QFA uses a combination of trace and rare earth elements (Co, Nb, Y, La, Ce, Eu, Yb, and Th) to explain 97% of the data variability with three factors (Fig. 2). The first aluminosilicate factor identified in the QFA

explained 45% of the variability in the dataset and indicated a strong covariance (i.e., high VARIMAX factor scores) among Nb, La, Ce, and Th throughout the samples (Fig. 2). The second factor explained 36% of the variability of the dataset and indicated a strong covariance among Y, Ce, Eu, and Yb. The third factor explained 16% of the dataset and showed a covariance between Co and Eu.

After testing thousands of different combinations of end-members in the CLS model to find the best fit for these element concentrations (Dunlea and Murray, 2015), QFA Factors 1-3 were interpreted to represent a continental dust source and two andesitic tephra end-members, respectively. In the CLS model, a continental dust end-member was chosen to approximate the composition of upper continental crust (Rudnick and Gao, 2013). This interpretation is in accord with previous studies that show Saharan dust forms a minor component of marine sediments in this area (Reid et al., 1996). The first andesitic tephra with a more felsic composition used in the model was a discrete tephra layer measured in this study (134.63 mbsf at Site U1396), but was also represented well by a subaerial tephra from Montserrat (Sample 11.1.4C from Coussens et al., 2017). The second andesitic tephra end-member with a more mafic composition than the other andesitic tephra layers is represented best by a tephra composition from the Las Sierra volcanoes in Nicaragua (Schindlbeck et al., 2018), but the composition is also similar to a subaerial tephra from Monserrat (Sample 9.2.1E from Coussens et al., 2017). Based on its proximity, subaerial tephra from Montserrat was selected as the more likely for Site U1396C (Fig. 3).

Previous work offshore Montserrat has indicated that sediments are a three-component mixture (terrestrial, $CaCO_3$ and tephra) and that Cr depletion can be used as a proxy for tephra content (Peters et al., 2000; Scudder et al., 2016). Our approach builds on this normative calculation, as it considers a range of elements. Our findings support previous work that indicates much of the tephra in marine sediments is not in discrete layers, but is in the ‘dispersed’ tephra component (Peters et al., 2000; Scudder et al., 2009; 2014). That is, tephra that has undergone some form of mixing process (e.g. bioturbation, transport in the water column) is not visible in sediment cores as discrete layers (Scudder et al., 2009; 2016). As expected, with ‘tephra layers’ (identified as layers with $CaCO_3$ <10 wt.%), the tephra component is typically >85 wt.% (89 ± 13 wt.%, 1SD, n=18). However, in the bulk sediment samples, the combined andesite tephra (i.e., the dispersed tephra component) contribution remains high

(29 ± 10 wt.%, 1 SD, n = 43), with a maximum of 55 wt.% (Fig. 3). An average of 29 wt.% is higher than the previous upper estimate of dispersed tephra in this region's sediment (between 15 – 20 wt.%; Peters et al., 2000), and confirms the importance of tephra deposition in Caribbean sediments.

Fe isotope systematics

The δ^{56}Fe values in tephra-rich samples from U1396C range from -0.26 to 0.01 ‰, with an average of -0.12 ± 0.08 ‰ (1SD, n=19). 18 of 19 samples fall outside of the range of crustal rocks (0.09 ± 0.07 ‰, as defined by Beard et al. 2003), and none have a δ^{56}Fe composition higher than these crustal rocks (Fig. 4, Supplementary Table 2). Our measured Fe isotope value of terrestrial tephra on Montserrat (δ^{56}Fe = -0.019 ± 0.02‰) is within the envelope of crustal rock compositions, and similar to previous measurements of volcanics from the Lesser Antilles , which yielded a δ^{56}Fe value of 0.045 ± 0.039‰ (Foden et al., 2018). These measurements on the Lesser Antilles volcanics were completed on lava samples from onshore outcrops, and so the comparability between the two values suggests little Fe isotope fractionation occurs during the eruption of explosive volcanic products in the Lesser Antilles arc. While airborne transport may alter Fe speciation (Maters et al., 2017) and total Fe content of the tephra (Simonella et al., 2015), atmospheric processes do not significantly alter the Fe isotope composition of the tephra.

Measurements of marine sediment and tephra samples from Hole U1396C, show considerable variation from what may be considered a magmatic rock Fe isotope composition, with subaerial volcanic rock isotope compositions typically between −0.054 and 0.1 ‰ (Foden et al., 2018; Johnson et al., 2020). Thus, our data indicate that some process within the tephra-rich sediments leads more negative δ^{56}Fe values in the tephras recovered from marine sediments than observed in subaerial volcanic rocks. This process may involve a diagenetic reaction, admixture of other sedimentary sources with distinct Fe isotopic compositions, and/or interaction with Fe from seawater.

To investigate the possibility that the total isotopic composition ($\delta^{56}Fe_{Total}$) reflects the mixture of tephra with terrigenous and carbonate contributions, we assume the isotopic composition is governed by the mass-balance of these sources ($\delta^{56}Fe_{ash,}$ $\delta^{56}Fe_{terr}$ and $\delta^{56}Fe_{carb}$, respectively; Eq. 3):

261 $$\delta^{56}Fe_{Total} = (\delta^{56}Fe_{Tephra} \times f_{Tephra}) + (\delta^{56}Fe_{terr} \times f_{terr}) + (\delta^{56}Fe_{Carb} \times f_{carb})$$ (Eq. 3)

262 Where f is the molar fraction of each component. However, as there is little evidence for any Fe-rich
263 carbonates such as siderite in the Caribbean Sea with only aragonite and Mg-rich carbonate reported
264 (Reid et al., 1996), this fraction is likely to contain low levels of Fe (Fe/Ca of below 30 μmol mol^{-1}; see
265 Boyle, 1981). Any Fe associated with the biogenic carbonate will be present only in the form of Fe-Mn
266 diagenetic coatings (Boyle, 1981). As such, we consider the carbonate contribution to the isotopic
267 mixture to be negligible, and so simplify the equation as follows (Eq. 4):

268 $$\delta^{56}Fe_{Total} = (\delta^{56}Fe_{Tephra} \times f_{Tephra}) + (\delta^{56}Fe_{terr} \times f_{terr})$$ (Eq. 4)

269 We can use our measured estimate of δ^{56}Fe for terrestrial tephra (-0.019 ± 0.023 ‰; $\delta^{56}Fe_{Tephra}$),
270 published estimates of the δ^{56}Fe of terrigenous material (c. 0.01 ± 0.05 ‰; $\delta^{56}Fe_{Terr}$, Beard et al., 2003),
271 and the proportion estimates for tephra (combining the contribution of the two andesites) and
272 terrigenous material (f_{Ash}, f_{Terr}) from the CLS model to assess if a simple mixture may explain the
273 measured Fe composition in our samples. Using the values of $\delta^{56}Fe_{Tephra}$ and $\delta^{56}Fe_{Terr}$ and the error
274 defined above, the most negative δ^{56}Fe composition produced by these mixtures is -0.043‰
275 (significantly more positive than most of the samples measured from U1396C).

276 One of the key diagenetic processes which acts on tephra in marine sediment is dissolution and leaching
277 (Jones and Gislason, 2008; Longman et al., 2019). Here, we focus on those 12 samples containing >75
278 wt.% ash (the closest representatives of 'pure' tephra samples within our sample suite) to test whether
279 diagenesis favours the loss of heavy Fe isotopes and the retention of isotopically light (δ^{56}Fe lower than
280 -0.1‰) Fe in the sediment. In this mass balance calculation, we assume that the measured δ^{56}Fe
281 ($\delta^{56}Fe_{Measured}$) is the result of the modification of the original tephra, with the Fe lost through early
282 diagenesis represented by the proportion f_{Lost}. In this scenario, the $\delta^{56}Fe_{Measured}$ comprises the following
283 mass balance (Eq. 5):

284 $$\delta^{56}Fe_{Measured} = (\delta^{56}Fe_{Tephra} \times f_{Tephra}) - (\delta^{56}Fe_{Lost} \times f_{Lost})$$ (Eq. 5)

285 The calculated $\delta^{56}Fe_{Lost}$ values, are considered representative of the isotopic composition of the Fe lost
286 during early diagenesis, and f_{Lost} is the proportion of Fe present in the protolith lost. f_{Lost} can be estimated
287 using depletion factor (DF_{Fe}) calculations (see Methods and Materials), which estimate how much of
288 the original Fe has been lost (using a Zr depletion model as detailed in Lee et al. (2018), and as second
289 CLS-based model, using outputs from the multivariate partitioning). Therefore, f_{Tephra} is calculated by
290 subtracting f_{Lost} from 1. By rearranging equation 5, and using these independent DF_{Fe} estimates as f_{Lost},
291 we can solve for $\delta^{56}Fe_{Lost}$ as follows:

292 $$\delta^{56}Fe_{Lost} = (\delta^{56}Fe_{ash} \times f_{Tephra}) - (\delta^{56}Fe_{Measured})/f_{Lost}$$ (Eq. 6)

293 As we use two methods to estimate DF_{Fe}, we derive two estimates for $\delta^{56}Fe_{Lost}$ (see Fig. 5), but they are
294 in good agreement (Supplementary Figure 2), with significant correlation between the two (r^2=0.65, p-
295 value 0.02, n=12), indicating both approaches yield similar outputs, although the ranges vary (CLS
296 Model -3 – 54%, Zr normalisation model -12 – 80%). Both approaches suggest generally positive values
297 for $\delta^{56}Fe_{Lost}$ relative to the original isotopic composition of the tephra. A single sample appears to have
298 gained Fe through diagenesis, potentially through reprecipitation of Fe-bearing phases, reflected in the
299 negative model result (Fig. 5). The results derived from Zr-normalisation show slightly higher mean
300 values for $\delta^{56}Fe_{Lost}$ (0.36 ± 0.28‰, 1SD, n=12) within uncertainty of the mean value derived from our
301 CLS modelling approach (0.21 ± 0.15‰, 1SD, n=12). These positive values for $\delta^{56}Fe$ are similar to
302 measurements of Fe supplied to porewater and seawater via non-reductive dissolution (NRD), as
303 inferred in oxidizing pore water $\delta^{56}Fe$ from tephra-rich sediments near the Crozet Islands (0.16 ±
304 0.05‰; Homoky et al., 2009), the Cape Margin (0.22‰; Homoky et al., 2013), South Western Atlantic
305 ($\delta^{56}Fe$ = 0.07 ± 0.07‰; Homoky et al., 2021) and New Guinea Coastal waters (0.37 ± 0.15‰; Radic et
306 al., 2011). It is assumed NRD does not truly represent a chemical reaction, rather a physical breakdown
307 of particles into smaller fractions, a process which should not lead to isotopic fractionation. However,
308 the binding of these small particles to ligands is known to fractionate the Fe, with shifts of between +0.2
309 to +0.5‰ observed experimentally (Dideriksen et al., 2008; Morgan et al., 2010) and in the natural
310 environment (Ilina et al., 2013). Therefore, it is likely the isotopic fractionation observed here is
311 representative of first the NRD breakdown of tephra particles, followed by a range of secondary

chemical reactions involving strong Fe-binding ligands, which fractionates the Fe. Such a process has been invoked to explain the positive δ^{56}Fe values observed in North Atlantic surface waters (between +0.3 to +0.7‰, despite the primary Fe source being dust (which typically has δ^{56}Fe values close to 0‰; Conway and John, 2014).

NRD of lithogenic particles occurs either during transport through the water column or at the sediment-seawater interface, and may occur in both oxic or dysoxic water column and/or pore water (Homoky et al., 2021, 2013; Radic et al., 2011). Thus, the rapid consumption of pore water oxygen observed in sediments offshore Montserrat (Hembury et al., 2012) does not preclude the occurrence of NRD. NRD results in a net release of isotopically heavy dissolved Fe (dFe with δ^{56}Fe > 0‰) to bottom water (Abadie et al., 2017; Labatut et al., 2014) or to seawater during transport through the water column (Labatut et al., 2014). Previous studies have shown that NRD may only result in small benthic Fe fluxes in some settings (Homoky et al., 2013), but fluxes out of the sediment may be enhanced in locations of high lithogenic (e.g. dust, riverine particles) deposition and/or sediment re-suspension (Klar et al., 2018; Labatut et al., 2014; Lam et al., 2020).

The regular and large-scale input of tephra from volcanoes in Central America (e.g. Schindlbeck et al., 2016), and the Lesser Antilles (Coussens et al., 2017; Palmer et al., 2016) provides a significant source of volcanic material for the Caribbean Sea. In a similar manner to western Africa, where input of lithogenic material via riverine input leads to a large supply of Fe from NRD (Klar et al., 2018), our data suggest the deposition of tephra in the Caribbean may act as a source of Fe, via NRD. Indeed, tephra is known to rapidly release Fe via interactions with seawater (Jones and Gislason, 2008), and during early diagenesis (Longman et al., 2022, 2019). This release from tephra is inferred from the relatively high Fe content in pore waters from U1396C (typical values between 10 – 50 μmol; Fig. 2), and dissolution of tephra is also reflected in the volcanogenic Sr isotope composition of the pore waters (Fig. 4; Murray et al., 2018).

Further evidence for release of dFe from tephra in the marine sediments comes from data from the Crozet Islands (Homoky et al., 2009). Here, the signal of NRD (and likely ligand binding) was identified in the Fe released to the pore water (with isotopic compositions between -0.01 and 0.12‰), and was

linked to high concentrations of colloidal Fe (Fe associated with particles between 1 – 1000 nm in size; cFe) (Homoky et al., 2011, 2009). Previous analysis of pore waters in the Caribbean has indicated that there is very little cFe relative to Crozet in fresh tephra layers collected from Montserrat previously. At Montserrat, <0.01 μmol cm^{-2} yr^{-1} of cFe is supplied to porewaters, whilst at Crozet cFe supply is calculated to be >1 μmol cm^{-2} yr^{-1} (Homoky et al., 2011). However, this absence of porewater Fe colloids in fresh tephra was shown to result from the undersaturation of Fe-bearing smectite clays (Homoky et al., 2011) and a lack of organic carbon to complex Fe nanominerals (Homoky et al., 2021). We argue therefore that the source of cFe to the seawater is release from dissolving volcanic tephra during transport through the water column and at the sediment-water interface. This conclusion is supported by the systematic offset between calculated $\delta^{56}Fe_{Lost}$ at Montserrat and the signature of Crozet pore waters of around 0.2 to 0.3‰. Evidence for the impact of NRD on regional Fe budgets may be identified in $\delta^{56}Fe$ compositions of western North Atlantic seawater. Measurements of seawater down to 4200 metres depth offshore Bermuda yielded $\delta^{56}Fe$ values between 0.2 to 0.74‰ (Conway and John, 2014; John and Adkins, 2012), which are within the range of our calculated $\delta^{56}Fe_{Lost}$ values (Fig. 5). As discussed above, these Fe isotope compositions have been attributed to a mixture of dust fractionation and organic ligand-mediated processes (Conway and John, 2014; John and Adkins, 2012; König et al., 2021). We also propose that input of dFe from tephra-rich sediment alteration may play a role in these isotopically heavy $\delta^{56}Fe$ values in the Bermudan samples by advection of extensive benthic nepheloid layers from the Caribbean and Gulf of Mexico (Feely, 1975; McCave, 1986), but analysis of Caribbean Sea seawater would be required to test this hypothesis.

Conclusions

We measured the major and trace element concentration and Fe isotopic composition of tephra and sediment layers from the Caribbean Sea. The bulk sediment is dominated by biogenic carbonate, but using a multivariate partitioning approach, we determined that aluminosilicate material in the sediment is a mixture of three primary sources, two linked to tephra deposition and one linked to terrestrial input. Overall, dispersed tephra comprises 29% of all sediment analyzed in this study. Fe isotope analyses indicate that tephra within the sediment, which has undergone water column transport and subsequent

diagenesis, has δ^{56}Fe values that are isotopically lighter than its source material, with δ^{56}Fe values as low as -0.26‰. This is considerably lighter than measured δ^{56}Fe from fresh tephra (which we show to be close to 0 ‰). Modelling of these Fe isotope data using multivariate partitioning suggests that the negative δ^{56}Fe values of sediment hosted tephra layers results from the loss of heavy Fe isotopes during tephra dissolution and diagenesis. This Fe loss most likely occurs as the result of non-reductive dissolution of the tephra. We suggest the release of this tephra-hosted Fe may play a considerable role in marine biogeochemical cycles such as the supply of nutrients for phytoplankton metabolism. Further, the deposition of volcanic material may have an impact on the mean Fe isotope composition of seawater in the vicinity of volcanoes.

Acknowledgements

This manuscript used samples provided by the Integrated Ocean Drilling Program (IODP) from Expedition 340. IODP is sponsored by the U.S. National Science Foundation (NSF). The authors are grateful to the co-chief scientists A. Le Friant and O. Ishizuka of Expedition 340 as well as all the participants in the expedition for their contributions to the sea-going effort. Appreciation is extended to Jesse Muratli at Oregon State University for his work in the laboratory. Financial support was provided by the United States Science Support Program (USSSP) and the US National Science Foundation to JM under grant Numbers 1360077 and 1715106 for shore-based analyses. MRP acknowledges NERC grant NE/K00543X/1 for financial support.

References

Abadie, C., Lacan, F., Radic, A., Pradoux, C., Poitrasson, F., 2017. Iron isotopes reveal distinct dissolved iron sources and pathways in the intermediate versus deep Southern Ocean. Proc. Natl. Acad. Sci. U. S. A. 114, 858–863. https://doi.org/10.1073/pnas.1603107114

Achterberg, E.P., Moore, C.M., Henson, S.A., Steigenberger, S., Stohl, A., Eckhardt, S., Avendano, L.C., Cassidy, M., Hembury, D., Klar, J.K., Lucas, M.I., Macey, A.I., Marsay, C.M., Ryan-Keogh, T.J., 2013. Natural iron fertilization by the Eyjafjallajökull volcanic eruption. Geophys. Res. Lett. 40, 921–926. https://doi.org/10.1002/grl.50221

Beard, B.L., Johnson, C.M., Von Damm, K.L., Poulson, R.L., 2003. Iron isotope constraints on Fe cycling and mass balance in oxygenated Earth oceans. Geology 31, 629–632. https://doi.org/10.1130/0091-7613(2003)031<0629:IICOFC>2.0.CO;2

Bennett, S.A., Rouxel, O., Schmidt, K., Garbe-Schönberg, D., Statham, P.J., German, C.R., 2009. Iron

396 isotope fractionation in a buoyant hydrothermal plume, 5°S Mid-Atlantic Ridge. Geochim.
397 Cosmochim. Acta 73, 5619–5634. https://doi.org/10.1016/J.GCA.2009.06.027

398 Böning, P., Brumsack, H.J., Böttcher, M.E., Schnetger, B., Kriete, C., Kallmeyer, J., Borchers, S.L.,
399 2004. Geochemistry of Peruvian near-surface sediments. Geochim. Cosmochim. Acta 68, 4429–
400 4451. https://doi.org/10.1016/j.gca.2004.04.027

401 Böning, P., Schnetger, B., Belz, L., Ferdelman, T., Brumsack, H.J., Pahnke, K., 2020. Sedimentary iron
402 cycling in the Benguela upwelling system off Namibia. Earth Planet. Sci. Lett. 538, 116212.
403 https://doi.org/10.1016/J.EPSL.2020.116212

404 Boyle, E.A., 1981. Cadmium, zinc, copper, and barium in foraminifera tests. Earth Planet. Sci. Lett. 53,
405 11–35. https://doi.org/10.1016/0012-821X(81)90022-4

406 Browning, T.J., Achterberg, E.P., Engel, A., Mawji, E., 2021. Manganese co-limitation of
407 phytoplankton growth and major nutrient drawdown in the Southern Ocean. Nat. Commun. 12,
408 1–9. https://doi.org/10.1038/s41467-021-21122-6

409 Browning, T.J., Bouman, H.A., Henderson, G.M., Mather, T.A., Pyle, D.M., Schlosser, C., Woodward,
410 E.M.S., Moore, C.M., 2014. Strong responses of Southern Ocean phytoplankton communities to
411 volcanic ash. Geophys. Res. Lett. 41, 2851–2857. https://doi.org/10.1002/2014GL059364

412 Conway, T.M., John, S.G., 2014. Quantification of dissolved iron sources to the North Atlantic Ocean.
413 Nature 511, 212–215. https://doi.org/10.1038/nature13482

414 Coussens, M., Cassidy, M., Watt, S.F.L., Jutzeler, M., Talling, P.J., Barfod, D., Gernon, T.M., Taylor,
415 R., Hatter, S.J., Palmer, M.R., 2017. Long-term changes in explosive and effusive behaviour at
416 andesitic arc volcanoes: Chronostratigraphy of the Centre Hills Volcano, Montserrat. J. Volcanol.
417 Geotherm. Res. 333–334, 15–35. https://doi.org/10.1016/j.jvolgeores.2017.01.003

418 Dauphas, N., Pourmand, A., Teng, F.Z., 2009. Routine isotopic analysis of iron by HR-MC-ICPMS:
419 How precise and how accurate? Chem. Geol. 267, 175–184.
420 https://doi.org/10.1016/J.CHEMGEO.2008.12.011

421 Dideriksen, K., Baker, J.A., Stipp, S.L.S., 2008. Equilibrium Fe isotope fractionation between inorganic
422 aqueous Fe(III) and the siderophore complex, Fe(III)-desferrioxamine B. Earth Planet. Sci. Lett.
423 269, 280–290. https://doi.org/10.1016/J.EPSL.2008.02.022

424 Duggen, S., Olgun, N., Croot, P., Hoffmann, L., Dietze, H., Delmelle, P., Teschner, C., 2010. The role
425 of airborne volcanic ash for the surface ocean biogeochemical iron-cycle: a review.
426 Biogeosciences 7, 827–844. https://doi.org/10.5194/bg-7-827-2010

427 Dunlea, A.G., Murray, R.W., 2015. Optimization of end-members used in multiple linear regression
428 geochemical mixing models. Geochemistry, Geophys. Geosystems 16, 4021–4027.
429 https://doi.org/10.1002/2015GC006132

430 Dunlea, A.G., Murray, R.W., Sauvage, J., Spivack, A.J., Harris, R.N., D'Hondt, S., 2015. Dust, volcanic
431 ash, and the evolution of the South Pacific Gyre through the Cenozoic. Paleoceanography 30,
432 1078–1099. https://doi.org/10.1002/2015PA002829

433 Falkowski, P.G., Barber, R.T., Smetacek, V., 1998. Biogeochemical controls and feedbacks on ocean
434 primary production. Science (80-.). https://doi.org/10.1126/science.281.5374.200

435 Feely, R.A., 1975. Major-element composition of the particulate matter in the near-bottom nepheloid
436 layer of the gulf of Mexico. Mar. Chem. 3, 121–156. https://doi.org/10.1016/0304-
437 4203(75)90019-5

438 Foden, J., Sossi, P.A., Nebel, O., 2018. Controls on the iron isotopic composition of global arc magmas.
439 Earth Planet. Sci. Lett. 494, 190–201. https://doi.org/10.1016/J.EPSL.2018.04.039

440 Frogner, P., Reynir Gíslason, S., Óskarsson, N., 2001. Fertilizing potential of volcanic ash in ocean

surface water. Geology 29, 487. https://doi.org/10.1130/0091-7613(2001)029<0487:FPOVAI>2.0.CO;2

Goñi, M.A., Teixeira, M.J., Perkeya, D.W., 2003. Sources and distribution of organic matter in a river-dominated estuary (Winyah Bay, SC, USA). Estuar. Coast. Shelf Sci. 57, 1023–1048. https://doi.org/10.1016/S0272-7714(03)00008-8

González De Vega, C., Chernonozhkin, S.M., Grigoryan, R., Costas-Rodríguez, M., Vanhaecke, F., 2020. Characterization of the new isotopic reference materials IRMM-524A and ERM-AE143 for Fe and Mg isotopic analysis of geological and biological samples. J. Anal. At. Spectrom. 35, 2517–2529. https://doi.org/10.1039/D0JA00225A

Hembury, D.J., Palmer, M.R., Fones, G.R., Mills, R.A., Marsh, R., Jones, M.T., 2012. Uptake of dissolved oxygen during marine diagenesis of fresh volcanic material. Geochim. Cosmochim. Acta 84, 353–368. https://doi.org/10.1016/J.GCA.2012.01.017

Homoky, W.B., Conway, T.M., John, S.G., König, D., Deng, F.F., Tagliabue, A., Mills, R.A., 2021. Iron colloids dominate sedimentary supply to the ocean interior. Proc. Natl. Acad. Sci. U. S. A. 118. https://doi.org/10.1073/PNAS.2016078118

Homoky, W.B., Hembury, D.J., Hepburn, L.E., Mills, R.A., Statham, P.J., Fones, G.R., Palmer, M.R., 2011. Iron and manganese diagenesis in deep sea volcanogenic sediments and the origins of pore water colloids. Geochim. Cosmochim. Acta 75, 5032–5048. https://doi.org/10.1016/J.GCA.2011.06.019

Homoky, W.B., John, S.G., Conway, T.M., Mills, R.A., 2013. Distinct iron isotopic signatures and supply from marine sediment dissolution. Nat. Commun. 4, 1–10. https://doi.org/10.1038/ncomms3143

Homoky, W.B., Severmann, S., Mills, R.A., Statham, P.J., Fones, G.R., 2009. Pore-fluid Fe isotopes reflect the extent of benthic Fe redox recycling: Evidence from continental shelf and deep-sea sediments. Geology 37, 751–754. https://doi.org/10.1130/G25731A.1

Ilina, S.M., Poitrasson, F., Lapitskiy, S.A., Alekhin, Y. V., Viers, J., Pokrovsky, O.S., 2013. Extreme iron isotope fractionation between colloids and particles of boreal and temperate organic-rich waters. Geochim. Cosmochim. Acta 101, 96–111. https://doi.org/10.1016/J.GCA.2012.10.023

John, S.G., Adkins, J., 2012. The vertical distribution of iron stable isotopes in the North Atlantic near Bermuda. Global Biogeochem. Cycles 26, 2034. https://doi.org/10.1029/2011GB004043

Johnson, C., Beard, B., Weyer, S., 2020. Iron Geochemistry: An Isotopic Perspective.

Jones, M.T., Gislason, S.R., 2008. Rapid releases of metal salts and nutrients following the deposition of volcanic ash into aqueous environments. Geochim. Cosmochim. Acta 72, 3661–3680. https://doi.org/10.1016/j.gca.2008.05.030

Klar, J.K., Schlosser, C., Milton, J.A., Woodward, E.M.S., Lacan, F., Parkinson, I.J., Achterberg, E.P., James, R.H., 2018. Sources of dissolved iron to oxygen minimum zone waters on the Senegalese continental margin in the tropical North Atlantic Ocean: Insights from iron isotopes. Geochim. Cosmochim. Acta 236, 60–78. https://doi.org/10.1016/j.gca.2018.02.031

Kolber, Z.S., Barber, R.T., Coale, K.H., Fitzwateri, S.E., Greene, R.M., Johnson, K.S., Lindley, S., Falkowski, P.G., 1994. Iron limitation of phytoplankton photosynthesis in the equatorial Pacific Ocean. Nature 371, 145–149. https://doi.org/10.1038/371145a0

König, D., Conway, T.M., Ellwood, M.J., Homoky, W.B., Tagliabue, A., 2021. Constraints on the Cycling of Iron Isotopes From a Global Ocean Model. Global Biogeochem. Cycles 35, e2021GB006968. https://doi.org/10.1029/2021GB006968

Labatut, M., Lacan, F., Pradoux, C., Chmeleff, J., Radic, A., Murray, J.W., Poitrasson, F., Johansen,

A.M., Thil, F., 2014. Iron sources and dissolved-particulate interactions in the seawater of the Western Equatorial Pacific, iron isotope perspectives. Global Biogeochem. Cycles 28, 1044–1065. https://doi.org/10.1002/2014GB004928

Lam, P.J., Heller, M.I., Lerner, P.E., Moffett, J.W., Buck, K.N., 2020. Unexpected Source and Transport of Iron from the Deep Peru Margin. ACS Earth Sp. Chem. 4, 977–992. https://doi.org/10.1021/ACSEARTHSPACECHEM.0C00066/ASSET/IMAGES/LARGE/SP0C00066_0009.JPEG

Le Friant, A., Ishizuka, O., Stroncik, N.A., Expedition 340 Scientists, T., 2013. Proc. IODP, 340. Integrated Ocean Drilling Program Management International, Inc., Tokyo.

Lee, C.-T.A., Jiang, H., Ronay, E., Minisini, D., Stiles, J., Neal, M., 2018. Volcanic ash as a driver of enhanced organic carbon burial in the Cretaceous. Sci. Rep. 8, 4197. https://doi.org/10.1038/s41598-018-22576-3

Liu, S.A., Teng, F.Z., Li, S., Wei, G.J., Ma, J.L., Li, D., 2014. Copper and iron isotope fractionation during weathering and pedogenesis: Insights from saprolite profiles. Geochim. Cosmochim. Acta 146, 59–75. https://doi.org/10.1016/J.GCA.2014.09.040

Longman, J., Mills, B.J.W., Manners, H.R., Gernon, T.M., Palmer, M.R., 2021. Late Ordovician climate change and extinctions driven by elevated volcanic nutrient supply. Nat. Geosci. 14, 924–929. https://doi.org/10.1038/s41561-021-00855-5

Longman, J., Palmer, M.R., Gernon, T.M., 2020. Viability of greenhouse gas removal via artificial addition of volcanic ash to the ocean. Anthropocene 32. https://doi.org/10.1016/j.ancene.2020.100264

Longman, J., Palmer, M.R., Gernon, T.M., Manners, H.R., 2019. The role of tephra in enhancing organic carbon preservation in marine sediments. Earth-Science Rev. 192, 480–490. https://doi.org/10.1016/j.earscirev.2019.03.018

Longman, J., Palmer, M.R., Gernon, T.M., Manners, H.R., Jones, M.T., 2022. Subaerial volcanism as a major contributor to oceanic iron and manganese cycles. Commun. Earth Environ.

Lough, A.J.M., Klar, J.K., Homoky, W.B., Comer-Warner, S.A., Milton, J.A., Connelly, D.P., James, R.H., Mills, R.A., 2017. Opposing authigenic controls on the isotopic signature of dissolved iron in hydrothermal plumes. Geochim. Cosmochim. Acta 202, 1–20. https://doi.org/10.1016/J.GCA.2016.12.022

Martin, J.H., Fitzwater, S.E., 1988. Iron deficiency limits phytoplankton growth in the north-east pacific subarctic. Nature 331, 341–343. https://doi.org/10.1038/331341a0

Maters, E.C., Delmelle, P., Gunnlaugsson, H.P., 2017. Controls on iron mobilisation from volcanic ash at low pH: Insights from dissolution experiments and Mössbauer spectroscopy. Chem. Geol. 449, 73–81. https://doi.org/10.1016/J.CHEMGEO.2016.11.036

McCave, I.N., 1986. Local and global aspects of the bottom nepheloid layers in the world ocean. Netherlands J. Sea Res. 20, 167–181. https://doi.org/10.1016/0077-7579(86)90040-2

Moore, C.M., Mills, M.M., Arrigo, K.R., Berman-Frank, I., Bopp, L., Boyd, P.W., Galbraith, E.D., Geider, R.J., Guieu, C., Jaccard, S.L., Jickells, T.D., La Roche, J., Lenton, T.M., Mahowald, N.M., Marañón, E., Marinov, I., Moore, J.K., Nakatsuka, T., Oschlies, A., Saito, M.A., Thingstad, T.F., Tsuda, A., Ulloa, O., 2013. Processes and patterns of oceanic nutrient limitation. Nat. Geosci. 6, 701–710. https://doi.org/10.1038/ngeo1765

Morgan, J.L.L., Wasylenki, L.E., Nuester, J., Anbar, A.D., 2010. Fe Isotope Fractionation during Equilibration of Fe−Organic Complexes. Environ. Sci. Technol. 44, 6095–6101. https://doi.org/10.1021/ES100906Z

Murray, N.A., McManus, J., Palmer, M.R., Haley, B., Manners, H., 2018. Diagenesis in tephra-rich sediments from the Lesser Antilles Volcanic Arc: Pore fluid constraints. Geochim. Cosmochim. Acta 228, 119–135. https://doi.org/10.1016/J.GCA.2018.02.039

Murray, N.A., Muratli, J.M., Hartwell, A.M., Manners, H., Megowan, M.R., Goñi, M., Palmer, M., McManus, J., 2016. Data report: dissolved minor element compositions, sediment major and minor element concentrations, and reactive iron and manganese data from the Lesser Antilles volcanic arc region, IODP Expedition 340 Sites U1394, U1395, U1396, U1399, and U1400. Proc. Integr. Ocean Drill. Progr. 340. https://doi.org/10.2204/iodp.proc.340.207.2016

Oeser, M., Weyer, S., Horn, I., Schuth, S., 2014. High-Precision Fe and Mg Isotope Ratios of Silicate Reference Glasses Determined In Situ by Femtosecond LA-MC-ICP-MS and by Solution Nebulisation MC-ICP-MS. Geostand. Geoanalytical Res. 38, 311–328. https://doi.org/10.1111/J.1751-908X.2014.00288.X

Olgun, N., Duggen, S., Croot, P.L., Delmelle, P., Dietze, H., Schacht, U., Óskarsson, N., Siebe, C., Auer, A., Garbe-Schönberg, D., 2011. Surface ocean iron fertilization: The role of airborne volcanic ash from subduction zone and hot spot volcanoes and related iron fluxes into the Pacific Ocean. Global Biogeochem. Cycles 25, n/a-n/a. https://doi.org/10.1029/2009GB003761

Olgun, N., Duggen, S., Langmann, B., Hort, M., Waythomas, C., Hoffmann, L., Croot, P., 2013. Geochemical evidence of oceanic iron fertilization by the Kasatochi volcanic eruption in 2008 and the potential impacts on Pacific sockeye salmon. Mar. Ecol. Prog. Ser. 488, 81–88. https://doi.org/10.3354/meps10403

Palmer, M.R., Hatter, S.J., Gernon, T.M., Taylor, R.N., Cassidy, M., Johnson, P., Le Friant, A., Ishizuka, O., 2016. Discovery of a large 2.4 Ma Plinian eruption of Basse-Terre, Guadeloupe, from the marine sediment record. Geology 44, 123–126. https://doi.org/10.1130/G37193.1

Peters, J.L., Murray, R.W., Sparks, J.W., Coleman, D.S., Leckie, R.M., Sigurdsson, H., Acton, G.D., Abrams, L.J., Bralower, T.J., Carey, S.N., Chaisson, W.P., Cotillon, P., Cunningham, A.D., D'Hondt, S.L., Droxler, A.W., Galbrun, B., Gonzalez, J., Haug, G.H., Kameo, K., King, J.W., Lind, I.L., Louvel, V., Lyons, T.W., Mutti, M., Myers, G., Pearce, R.B., Pearson, D.G., Peterson, L.C., Roehl, U., 2000. Terrigenous matter and dispersed ash in sediment from the Caribbean Sea; results from Leg 165. Proc. Ocean Drill. Program, Sci. Results 165, 115–124. https://doi.org/10.2973/odp.proc.sr.165.003.2000

Pisias, N.G., Murray, R.W., Scudder, R.P., 2013. Multivariate statistical analysis and partitioning of sedimentary geochemical data sets: General principles and specific MATLAB scripts. Geochemistry, Geophys. Geosystems 14, 4015–4020. https://doi.org/10.1002/ggge.20247

Pyle, D.M., 1995. Mass and energy budgets of explosive volcanic eruptions. Geophys. Res. Lett. 22, 563–566. https://doi.org/10.1029/95GL00052

Radic, A., Lacan, F., Murray, J.W., 2011. Iron isotopes in the seawater of the equatorial Pacific Ocean: New constraints for the oceanic iron cycle. Earth Planet. Sci. Lett. 306, 1–10. https://doi.org/10.1016/j.epsl.2011.03.015

Reid, R.P., Carey, S.N., Ross, D.R., 1996. Late Quaternary sedimentation in the Lesser Antilles island arc. Bull. Geol. Soc. Am. 108, 78–100. https://doi.org/10.1130/0016-7606(1996)108<0078:LQSITL>2.3.CO;2

Rudnick, R.L., Gao, S., 2013. Composition of the Continental Crust. Treatise Geochemistry Second Ed. 4, 1–51. https://doi.org/10.1016/B978-0-08-095975-7.00301-6

Schindlbeck, J.C., Kutterolf, S., Freundt, A., Alvarado, G.E., Wang, K. -L., Straub, S.M., Hemming, S.R., Frische, M., Woodhead, J.D., 2016. Late Cenozoic tephrostratigraphy offshore the southern Central American Volcanic Arc: 1. Tephra ages and provenance. Geochemistry, Geophys. Geosystems 17, 4641–4668. https://doi.org/10.1002/2016GC006503@10.1002/(ISSN)1525-

2027.SUBDUCT2

Schindlbeck, J.C., Kutterolf, S., Freundt, A., Eisele, S., Wang, K.-L., Frische, M., 2018. Miocene to Holocene Marine Tephrostratigraphy Offshore Northern Central America and Southern Mexico: Pulsed Activity of Known Volcanic Complexes. Geochemistry, Geophys. Geosystems 19, 4143–4173. https://doi.org/10.1029/2018GC007832

Schoenberg, R., Von Blanckenburg, F., 2005. An assessment of the accuracy of stable Fe isotope ratio measurements on samples with organic and inorganic matrices by high-resolution multicollector ICP-MS. Int. J. Mass Spectrom. 242, 257–272. https://doi.org/10.1016/J.IJMS.2004.11.025

Scudder, R.P., Murray, R.W., Plank, T., 2009. Dispersed ash in deeply buried sediment from the northwest Pacific Ocean: An example from the Izu–Bonin arc (ODP Site 1149). Earth Planet. Sci. Lett. 284, 639–648. https://doi.org/10.1016/J.EPSL.2009.05.037

Scudder, R.P., Murray, R.W., Schindlbeck, J.C., Kutterolf, S., Hauff, F., McKinley, C.C., 2014. Regional-scale input of dispersed and discrete volcanic ash to the Izu-Bonin and Mariana subduction zones. Geochemistry, Geophys. Geosystems 15, 4369–4379. https://doi.org/10.1002/2014GC005561

Scudder, R.P., Murray, R.W., Schindlbeck, J.C., Kutterolf, S., Hauff, F., Underwood, M.B., Gwizd, S., Lauzon, R., McKinley, C.C., 2016. Geochemical approaches to the quantification of dispersed volcanic ash in marine sediment. Prog. Earth Planet. Sci. 3, 1. https://doi.org/10.1186/s40645-015-0077-y

Simonella, L.E., Palomeque, M.E., Croot, P.L., Stein, A., Kupczewski, M., Rosales, A., Montes, M.L., Colombo, F., García, M.G., Villarosa, G., Gaiero, D.M., 2015. Soluble iron inputs to the Southern Ocean through recent andesitic to rhyolitic volcanic ash eruptions from the Patagonian Andes. Global Biogeochem. Cycles 29, 1125–1144. https://doi.org/10.1002/2015GB005177

Tagliabue, A., Aumont, O., Death, R., Dunne, J.P., Dutkiewicz, S., Galbraith, E., Misumi, K., Moore, J.K., Ridgwell, A., Sherman, E., Stock, C., Vichi, M., Völker, C., Yool, A., 2016. How well do global ocean biogeochemistry models simulate dissolved iron distributions? Global Biogeochem. Cycles 30, 149–174. https://doi.org/10.1002/2015GB005289

Tagliabue, A., Bowie, A.R., Boyd, P.W., Buck, K.N., Johnson, K.S., Saito, M.A., 2017. The integral role of iron in ocean biogeochemistry. Nature. https://doi.org/10.1038/nature21058

Weyer, S., Schwieters, J.B., 2003. High precision Fe isotope measurements with high mass resolution MC-ICPMS. Int. J. Mass Spectrom. 226, 355–368. https://doi.org/10.1016/S1387-3806(03)00078-2

Figures

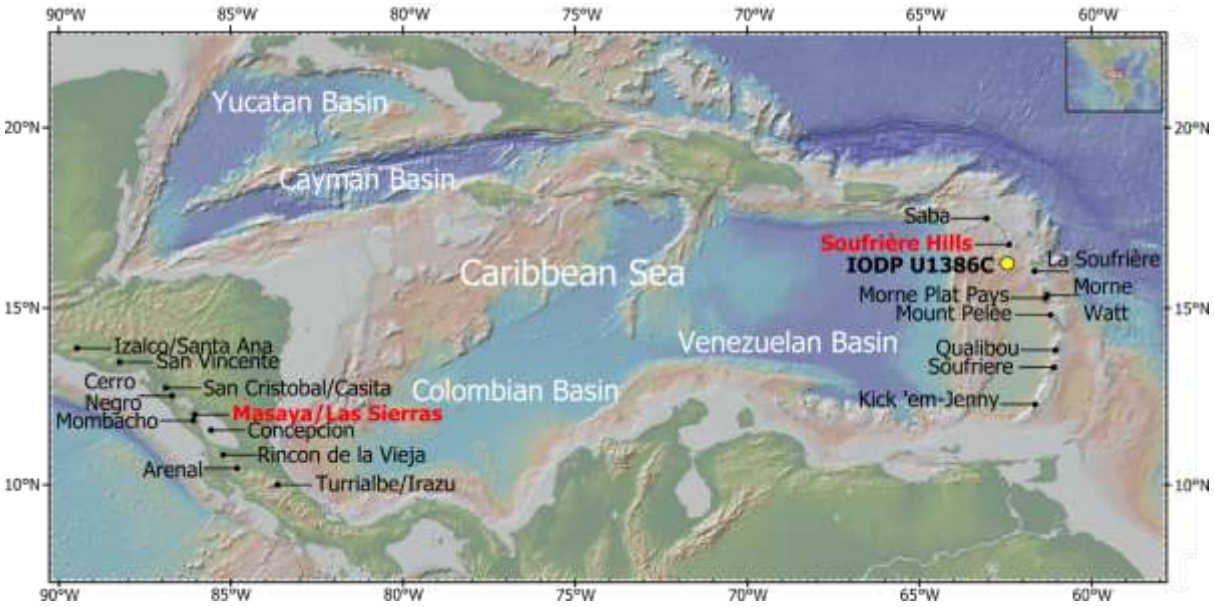

Figure 1: Map indicating location of Hole U1396C (yellow circle) within the Caribbean Sea area. Also shown are the locations of the primary recently active volcanoes in the region. The location of Las Sierras, and Soufrière Hills volcanoes, used in the modelling here, are indicated by bold red text. Map created in ArcMap 10.3, Environmental Systems Resource Institute, ArcMap 10.3 ESRI, Redlands, California, http://desktop.arcgis.com/en/arcmap/.

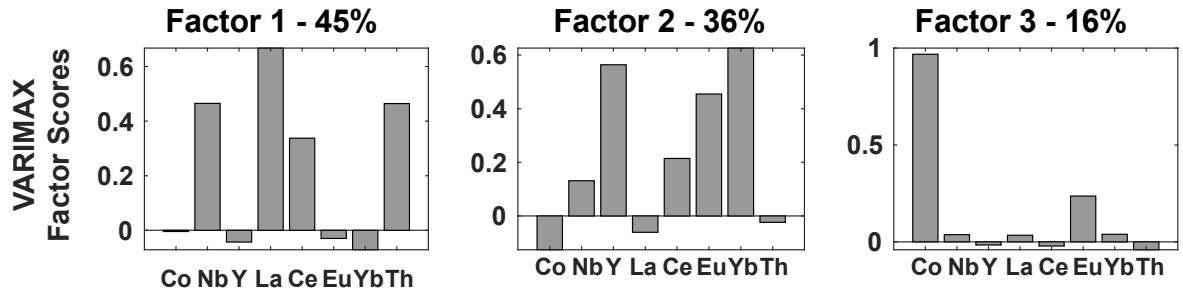

Figure 2: The VARIMAX factor scores from the Q-mode factor analysis. Elements affiliated with the aluminosilicate fraction produced three factors that explain 97% of the variability of the dataset (45%, 36%, and 16%, respectively).

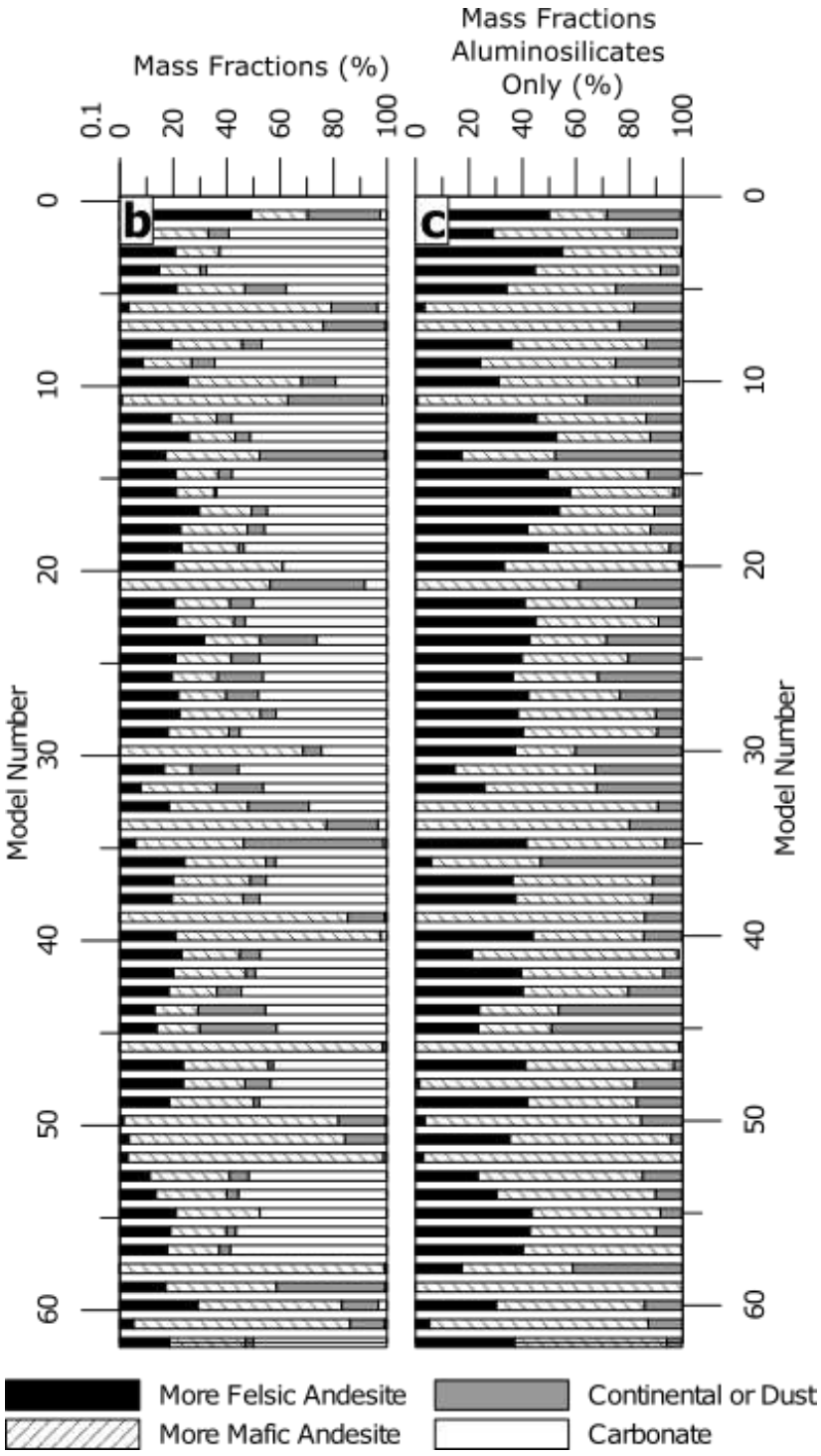

621

622 Figure 3: a) The results of the CLS model. Modelled end-member mass fractions in each discrete layer
623 or bulk sediment sample plotted with the same scale as panel a. Black and hashed white indicate the
624 mass fractions of the more felsic and more mafic andesites, respectively. Grey represents contributions
625 from an upper continental crust or dust source. The remaining white area represents the carbonate

626 fraction of bulk sediment. b) The CLS modelled mass fractions of only the aluminosilicate fraction of
627 the samples (excluding the carbonate fraction).

628

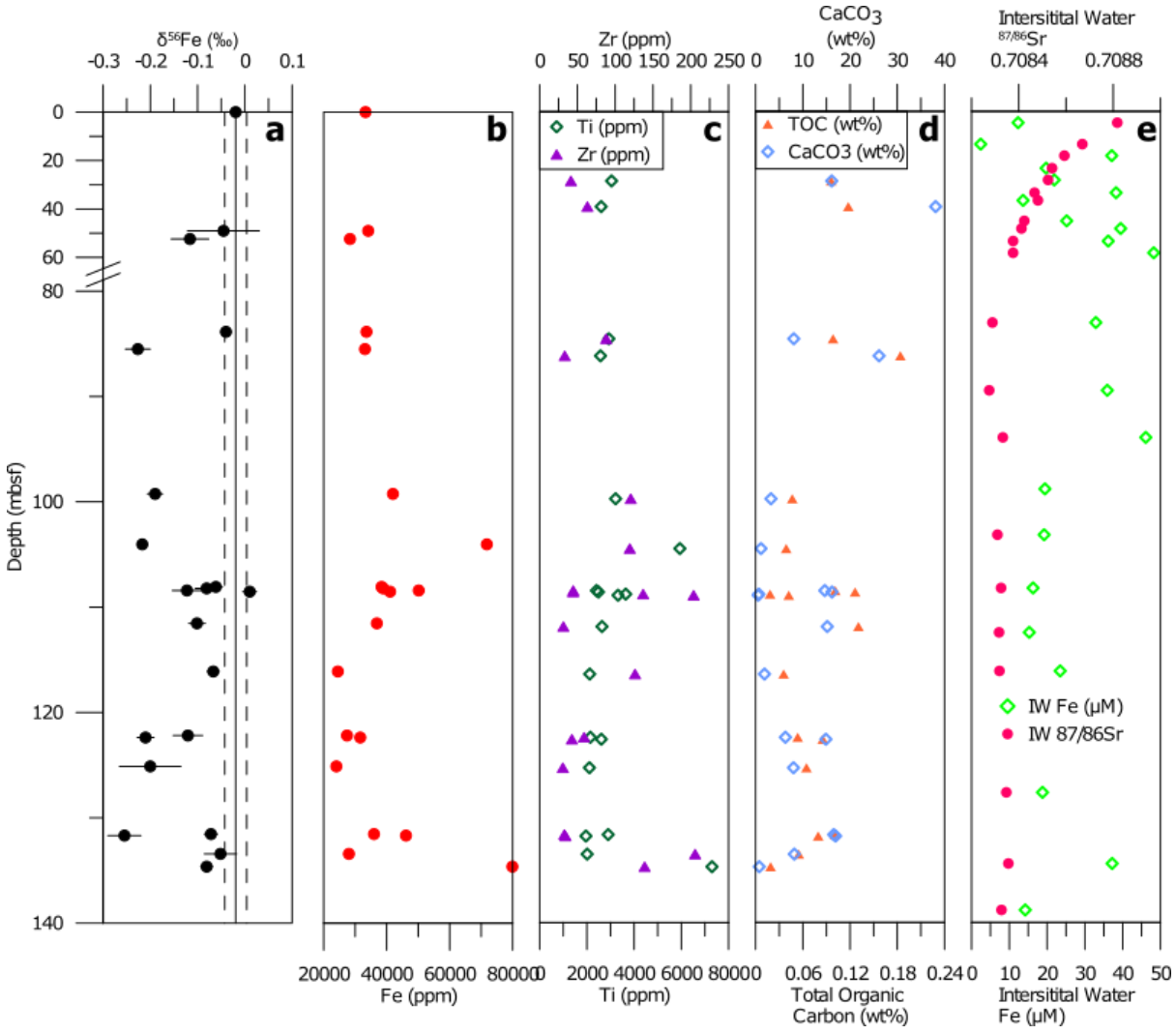

629

630 Figure 4: Geochemical parameters from U1396C. (a) Fe isotope composition of analysed samples, with
631 error bars indicating measurement error (2SD). The measured value of terrestrially emplaced ash from
632 Montserrat indicated with a black line, with measurement error indicated by dashed lines. (b) Fe content
633 of samples analysed for isotopic composition. (c) Ti and Zr content for the same samples. (d) calcium
634 carbonate and organic carbon (total carbon) content for the same samples. (e) Interstitial water Fe
635 content and Sr isotope composition (from Murray et al., 2018).

636

637

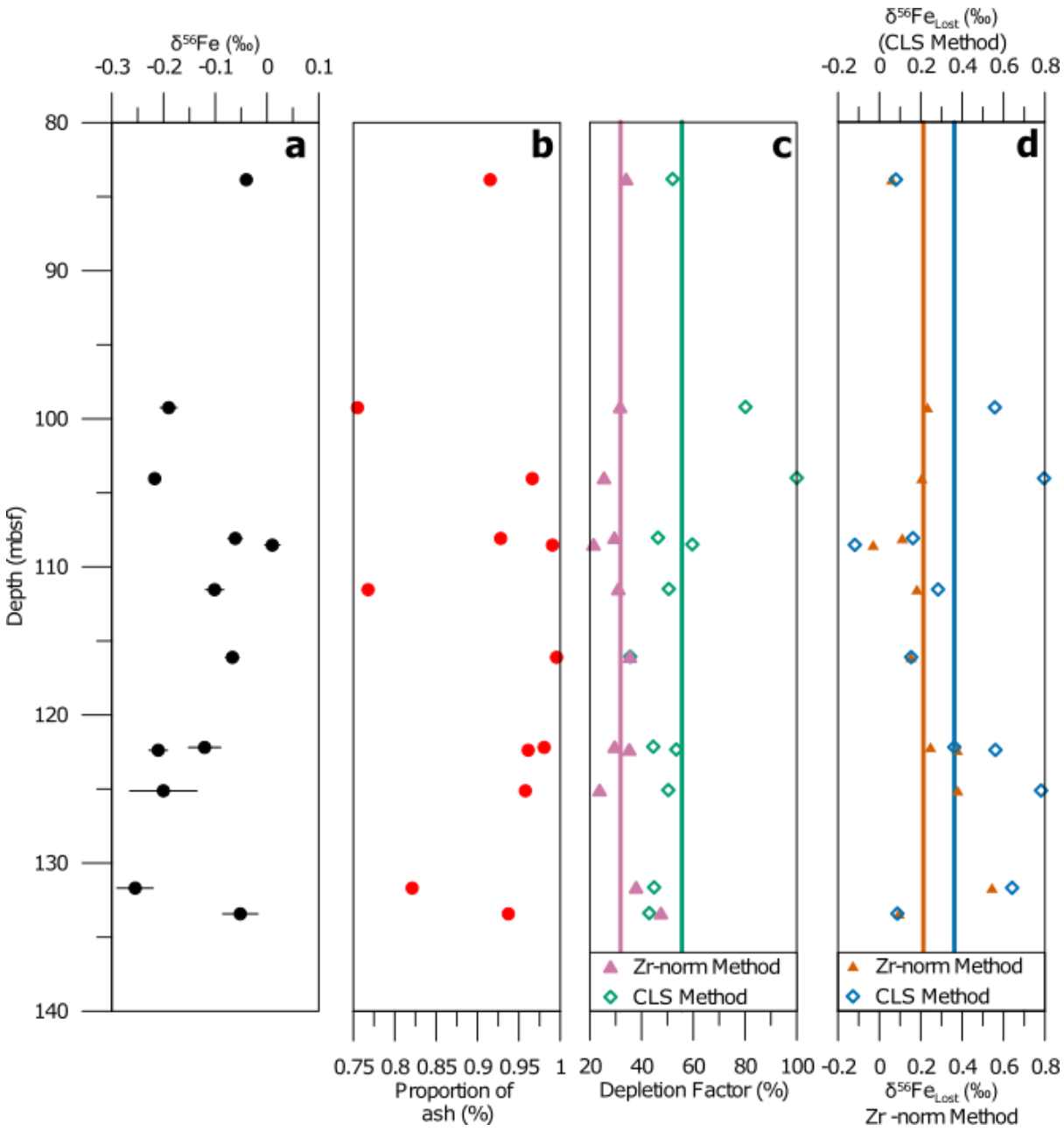

638

639 Figure 5: Parameters used in the mass balance modelling of the lost Fe fraction ($\delta^{56}Fe_{Lost}$), or the isotopic
640 composition of Fe flux from samples with >75% tephra. (a) Bulk $\delta^{56}Fe$ measurements for the samples
641 with high enough ash content to be modelled (>75%). (b) The proportion of ash in each sample, as
642 calculated from the multivariate modelling. (c) Fe depletion factor (DF) calculations, DF Method 1
643 from Lee et al. (2018) and DF Method 2 from our multivariate partitioning. Individual models are
644 indicated with coloured symbols, and the mean of each method is highlighted with a coloured line. (d)

The calculated $\delta^{56}Fe_{Lost}$ for each of the samples, with the calculations made using the depletion factors displayed in panel c. Again, the mean of the outputs is highlighted with a coloured line.